UACJ Technical Reports, Vol.10 (2023), pp. 60-74

Paper

On the Extraordinary Low Quench Sensitivity of an AlZnMg Alloy*

Christian Rowolt**,***, Benjamin Milkereit**,***,********, Armin Springer****, Mami Mihara-Narita*****, Hideo Yoshida******, Kenya Yamashita*******, Kevin Oldenburg********, and Olaf Kessler**,***,********

The scope of this work was to investigate the quench sensitivity of a high-purity wrought aluminum alloy Al-6%Zn-0.75%Mg (in this work called 7003_{pure}). This is compared to a similar alloy with the additions of Fe, Si, and Zr at a sum less than 0.3at.% (in this work called $7003_{Fe,Si,Zr}$). Differential scanning calorimetry (DSC) was used for an in situ analysis of quench induced precipitation in a wide range of cooling rates varying between 0.0003 and 3 K/s. In 7003_{pure}, three main precipitation reactions were observed during cooling, a medium temperature reaction with a distinct double peak between 325 and 175 ℃ and a very low temperature reaction starting at about 100 ℃. An additional high temperature reaction related to the precipitation of Mg_2Si starting at 425 ℃ has been observed for $7003_{Fe,Si,Zr}$. In terms of hardness after natural as well as artificial aging, alloy 7003_{pure} shows a very low quench sensitivity. Hardness values on the saturation level of about 120 HV1 are seen down to cooling rates of 0.003 K/s. The as-quenched hardness (5 min of natural aging) shows a maximum at a cooling rate of 0.003 K/s, while slower and faster cooling results in a lower hardness. In terms of hardness after aging, 0.003 K/s could be defined as the technological critical cooling rate, which is much higher for $7003_{Fe,Si,Zr}$ (0.3–1 K/s). The physical critical cooling rates for the suppression of any precipitation during cooling were found to be about 10 K/s for both variantsthe development of the very low temperature reaction seen by DSC and indicates a direct hardening contribution of the phase/particles precipitated during the this reaction upon cooling. High resolution scanning transmission electron microscopy reveals an enormous number density of clusters or GP zones with dimensions of about 3 to 5 nm after cooling at 0.003 K/s and additional natural aging. The physical critical cooling rate for the complete supersaturation of the solid solution was found to be about 10 K/s for the both variants.

Keywords: *quench sensitivity, differential scanning calorimetry (DSC), Al-Zn-Mg alloy, 7003, continuous cooling precipitation, STEM*

1. Introduction

Alloys from the system Al-Zn-Mg (7000 series alloys) combine high strength with low weight as well as good formability, which are important features for applications in the transportation industry, such as aerospace, automotive, or trains [1), 2)]. To adjust the strength of 7000 series alloys, the heat treatment precipitation hardening consisting of solution annealing, quenching, and aging is conducted [3)]. During solution annealing, the alloying elements are being dissolved and homogeneously distributed in the aluminum matrix followed by a more or less rapid quenching to room temperature. The latter typically aims to result in a fully supersaturated solid solution. In the last step, the material will be aged to promote

* This paper was reprinted from J. Mater. Sci. **56** (2021), 20181-20196.
** Chair of Materials Science, Faculty of Mechanical Engineering and Marine Technology, University of Rostock, Ph. D.
*** Competence Centre CALOR, Department Life, Light & Matter, University of Rostock, Ph. D.
**** Electron Microscopic Centre, University Medical Centre Rostock, Ph. D.
***** Department of Physical Science and Engineering, Nagoya Institute of Technology, Ph. D.
****** ESD Laboratory, Dr. Eng. (Formerly, Adviser, Research & Development Division, UACJ Corporation)
******* Furukawa UACJ Memory Disk Co., Ltd., Ph. D.
******** Centre for Interdisciplinary Electron-Microscopy (ELMI-MV), Department Life, Light and Matter, University of Rostock, Ph. D.

the formation of a high number density of nanoscaled precipitates. These hinder dislocation glide and thereby significantly increase the yield strength. In this process, quenching is a critical technological step. On the one hand, quenching has to be fast enough to fully suppress precipitation during cooling to achieve high strength after aging. On the other hand, excess residual stresses and distortion due to rapid quenching must be avoided. The reduction in properties (e.g., strength, ductility, toughness, corrosion resistance) due to falling cooling rates (i.e., quench-induced precipitation) is described by the term quench sensitivity [4)~6)].

In 1965, Baba applied for a patent for an Al-Zn-Mg alloy with zirconium added instead of chromium. He developed Al-Zn-Mg alloys with zirconium added for the first time named Sumitomo Alloy ZK47, ZK141. These alloys have been put into practical use as 7N01 (now 7204). In 1967, Sumitomo Alloy ZK60 (now 7003) was developed with a reduced amount of Mg and improved extrudability [7)~9)]. It can be extruded with direct air-cooling at press-outlet to obtain medium-strength [10)~13)]. This alloy has been registered with AA (The Aluminum Association) as 7003 in 1975. Zirconium was added for the first time instead of chromium as a dispersoid forming element [8), 9)]. Finally, it was used for Series 200 Shinkansen structures as well as motorcycle frames and rims. Yoshida et al. investigated the relationship between the ingot homogenization conditions and mechanical properties of zirconium added alloys [14)]. It was found that the addition of approximately 0.2mass% zirconium improves the strength and stress corrosion resistance. Zirconium as an alloying element leads to the formation of spherical dispersoids Al_3Zr during homogenization. However, this results in a higher quench sensitivity since the crystal-lattice misfit between the aluminum matrix and dispersoids favors the precipitation of η-$MgZn_2$ during cooling. Meanwhile, Al_3Zr dispersoids are reported to act as nucleation sites for quench-induced η-$MgZn_2$ or η-$Mg(Zn,Cu,Al)_2$ formation in multiple AlZnMg(Cu) alloys at least in the case that they have an incoherent interface with the matrix [4), 6), 15), 16)]. The addition of iron and silicon to 7003 results in coarse intermetallic particles enriched in Al, Si, and Fe [17)], which likely form as primary particles in the melt. Those types of intermetallic particles are also known to act as nucleation sites for quench-induced precipitates at high temperatures for a broad range of technical Al alloys [6)], particularly β-Mg_2Si nucleates on these coarse Al-Si-Fe-rich intermetallics [17)].

In Ref. 8), Baba also reported on the Vickers hardness of a "pure" variation of alloy 7003 containing only the alloying elements magnesium and zinc. He observed a very low quench sensitivity, as this "pure" alloy reached about 94% of the maximum hardness for slow cooling (0.025 K/s) from the solution annealing temperature compared to water quenched samples after artificial aging at 120 ℃ [8)]. Later, Yoshida et al. found that in this "pure" alloy under certain conditions, the hardness of furnace cooled samples is even higher than that of water quenched samples [18)].

The scope of this work is to further investigate the quench sensitivity and the mechanism of quench-induced precipitation (QIP) of this high wrought purity aluminum alloy Al-6%Zn-0.75%Mg (7003_{pure}) in comparison with a variant with the additions of Fe, Si, and Zr. Differential scanning calorimetry (DSC) is accompanied by hardness tests as well as extensive micro- and nano-structural investigations.

2. Materials and methods

The alloy 7003_{pure} was produced by the UACJ, Japan. Samples for this work were prepared out of an extruded rod with a diameter of 20 mm and a length of 200 mm. After casting, the material was homogenized at 500 ℃ for 8 h, and extrusion was done after heating to 400 ℃. **Table 1** shows the mass and atomic fractions of the alloying elements in the 7003_{pure} samples as determined by optical emission spectroscopy (OES).

In addition to the comprehensive investigation on 7003_{pure}, at some points, a direct comparison with a commercially extruded profile $7003_{Fe,Si,Zr}$ will be discussed. The main difference between both alloys is the amount of Fe, Si, and Zr (in sum less than 0.3at.%, see **Tables** 1 and **2**).

DSC cooling experiments were performed and evaluated regarding the specific excess heat capacity

Table 1 Fractions of alloying elements in 7003_{pure} according to optical emission spectroscopy.

	Si	Fe	Cu	Mn	Mg	Cr	Zn	Ti	Zr	Al
mass%	0.01	0.02	<0.01	<0.001	0.77	<0.001	6.1	<0.01	–	bal.
at.%	0.01	0.01	<0.01	<0.001	0.89	<0.001	2.61	<0.01	–	bal.

Table 2 Fractions of alloying elements in $7003_{Fe,Si,Zr}$ according to optical emission spectroscopy.

	Si	Fe	Cu	Mn	Mg	Cr	Zn	Ti	Zr	Al
mass%	0.11	0.2	0.01	–	0.68	–	5.56	0.02	0.17	bal.
at.%	0.11	0.1	0.00(4)	–	0.78	–	2.37	0.01	0.05	bal.

according to Ref. 19). The cooling rates were varied in a wide range from 0.0003 K/s to 1 K/s to comprehensively analyze the solid–solid phase transformation behavior. The following three different DSC devices were used to cover this enormous cooling rate range by in situ cooling DSC along with each specific sample size and sample mass:

• Setaram C600 (heat flow DSC): Ø 13.8 × 60.5 mm ≈ 24,700 mg

• Setaram Sensys & DSC121 (heat flow DSC): Ø 6 × 21.65 mm ≈ 1700 mg

• Perkin Elmer Pyris Diamond (power compensated DSC): Ø 6.4 × 1 mm ≈ 90 mg.

In the case of the faster cooling rates realized in the Perkin Elmer Pyris Diamond DSC, linear cooling was done down to −50 ℃, while slower cooling experiments ended at about 20 ℃.

To obtain additional information on the effect of varying cooling rates on the subsequent mechanical properties, Vickers hardness tests HV1 (ISO 6507) were carried out using a Shimadzu type HMV-2 micro hardness tester on the solution annealed and quenched samples as well as in aged conditions. "As-quenched "-condition means about 5 min after the end of cooling. The hardness was tested after 7, 28, 245, and 365 days of natural aging. Additionally, artificially aging, i.e., cooling from solution treatment at distinct rates, for 5 min at room temperature and aging at 120 ℃ for 24 h was compared. Samples for the hardness tests and microstructure investigations were solution annealed and quenched in a Perkin Elmer Pyris Diamond DSC (cooling rates: 0.0003-1 K/s). Faster cooling was achieved with a Bähr DIL 805 A/D quenching dilatometer (cooling rates: 3–100 K/s). For this purpose, cylindrical samples with a diameter of 6.4 mm and a length of 1 mm were used. To analyze the changes in the microstructure related to the reactions detected in DSC, optical microscopy (OM) as well as scanning electron microscopy (SEM) and energy-dispersive X-ray spectroscopy (EDS) were performed. The heat-treated samples were cold-embedded in epoxy resin and then mechanically ground and polished with water-free lubricants. The final polishing was done with a 0.05 µm polishing suspension. The polished samples were rinsed and etched as per Weck (4 g potassium permanganate $KMnO_4$, 1 g caustic soda NaOH, 100 ml water H_2O) [20].

The SEM samples were analyzed by a field emission SEM (MERLIN®VP Compact, Co. Zeiss, Ober-kochen, Germany) equipped with an EDS detector (XFlash 6/30) and analysis software (Quantax400, Co. Bruker, Berlin, Germany). The embedded and polished samples were mounted on the SEM carrier with adhesive conductive carbon and aluminum tape (Co. PLANO, Wetzlar, Germany). SEM-secondary electron (SEM-SE) images were obtained using a high efficiency Everhart-Thornley-type HE-SE detector at 5 kV acceleration voltage. Representative areas of the samples were analyzed and mapped to determine the elemental distribution on the basis of the EDS spectra data by the QUANTAX ESPRIT Microanalysis software (version 2.0). The acceleration voltage for the EDS analysis was set to 20 kV.

A Bruker Discover D8 X-ray diffractometer was applied to identify relevant phases after very slow cooling at 0.0003 K/s. The diffractometer was equipped with a Cu Kα source of wavelength 0.15406 nm using 40 kV and 40 mA. In detail, a step size of 0.04° with a measuring time per angular step of 1.4 s from 20 to 120 ℃ was set to collect the data.

The nanostructure of the slowly cooled and naturally aged samples was investigated in an analytical, probe aberration corrected scanning

transmission electron microscope (STEM) JOEL JEM-ARM200F NEOARM equipped with a cold field emission gun operated at 200 kV acceleration voltage. Images were acquired by a high-angle annular dark field detector (HAADF), and the chemical composition of relevant features were analyzed by a JEOL energy-dispersive X-ray (EDS) detector with an area of 100 mm^2.

For TEM, a thin disk of about 300 µm thickness was cut from the DSC sample by a diamond precision saw. This disk was ground and polished to a thickness of about 80 µm. The final electrolytical thinning was done by a STRUERS Tenupol 5 operated at −30 ℃ using an electrolyte consisting of 65-85% ethanol C_2H_6O, 10-15% 2-butoxy-ethanol $C_6H_{14}O_2$, and 5-15% water H_2O.

3. Results and Discussion

3.1 Quench-induced precipitation analyzed by in situ cooling DSC

Fig. 1 shows the DSC mean curves from multiple cooling experiments after annealing at 450 ℃ for 120 min (Setaram C600) or 60 min (Setaram Sensys DSC, Setaram DSC121 and Perkin Elmer Pyris Diamond DSC), respectively, over the broad dynamic range of four orders of magnitude from 0.0003 K/s to 1 K/s for 7003_{pure}. In terms of cooling durations, this means a variation of cooling from 450 to 25 ℃ within a range of about 16 days to just 7 min. The DSC curves are shifted above each other starting with the slowest cooling rate on top. For each DSC curve, its own zero level is plotted as a dotted straight line. Deviations of the DSC curve above the zero level indicate exothermic precipitation reactions. For 7003_{pure}, DSC reveals two main temperature regions of QIP:

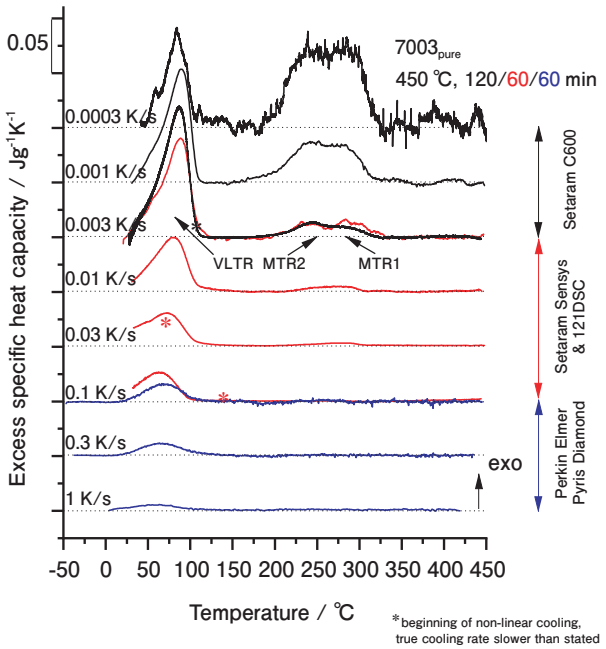

Fig. 1 Selected DSC cooling curves of 7003_{pure} covering four orders of magnitude of cooling rates from 0.0003 to 1 K/s.

- Medium-temperature precipitation (MTR) occurring in a double peak event from about 330 ℃ to 175 ℃ and
- A very low-temperature precipitation (VLTR) from about 110 ℃ down to 10 ℃.

As seen by the decreasing peak area, which is quantified as the specific precipitation enthalpy, plotted in **Fig. 3**(a), the MTR reactions are increasingly suppressed with increasing cooling rate. By cooling at 0.0003 K/s, the MTR releases a specific precipitation enthalpy of nearly 7 J/g. When cooling at 0.03 K/s, just a little more than 0.1 J/g (detection limit [6]) is released, and the reactions are virtually fully suppressed at 0.1 K/s.

The precipitation enthalpy of the VLTR starting from about 3 J/g at 0.0003 K/s first slightly increases. During cooling at 0.001 and 0.003 K/s, the VLTR releases about 3.5 J/g. At 0.003 K/s, the MTR is already suppressed to a wide extent. This indicates that the MTR and the VLTR compete on the same alloying element atoms. At a cooling rate of 1 K/s, the VLTR in 7003_{pure} still releases about 0.3 J/g, i.e., from DSC, it is seen that the critical cooling rate for a complete suppression of QIP is above 1 K/s for 7003_{pure}.

At this point, a side aspect from the DSC methodology should be discussed: each individual DSC device has its own upper and lower cooling rate limit [6]. At cooling rates close to its upper cooling rate limit, at a certain temperature the DSC will lose control about the programmed cooling rate and cooling will proceed slower afterward. Subsequent to this loss of control, only heat flux DSCs are still able to measure a heat flow signal. In most of our previous research (e.g. [6]), we cut off the nonlinear parts due to multiple reasons. One reason is that typically the

programmed cooling rate is taken as the value for the normalization of the heat flow toward the unit of heat capacity. This normalization allows the different scanning rates to be compared. Taking the above considerations, it is a challenge to analyze the VLTR by DSC, and it is noteworthy that we, here, used the true, effective cooling rate (derivative of the sample temperature) for normalization. The temperatures where cooling switches from linear cooling to nonlinear cooling are identified by an asterisk in Figs 1 and 2. From Fig. 1, it can be seen that we did the cooling experiments at 0.003 and 0.1 K/s in two overlapping DSC devices. Generally, a good match of the DSC curves at rates covered by the two devices is found. The noise level is, as usual, better for the device-specific fast cooling rate. Considering the VLTR peak, the slight differences that occur between the two used DSC devices are obvious. Basically, the DSC, which loses temperature control before the VLTR, measures a higher peak maximum and peak area. This is reasonable, as the slower cooling should result in a more pronounced precipitation reaction as more time is available for the diffusion to occur. Summarizing this part of the discussion, we consider it reasonable to allow for non-linear cooling at faster cooling rates and low temperatures in heat flux DSCs in order to assess such low temperature processes like the VLTR. This might be considered for the future design of cooling DSC experiments.

Fig. 2 plots the DSC cooling curves of $7003_{Fe,Si,Zr}$. The DSC data given in Fig. 2 have been published before [17]; however, here, we re-evaluated it to present an enlarged temperature range and an improved assessment of the VLTR. The addition of Fe, Si and Zr in a sum less than 0.3at.% obviously makes a huge impact on the QIP. This is seen from two aspects:

- Firstly, an additional high-temperature reaction HTR (about 410 to 310 ℃ at 0.01 K/s) is seen in $7003_{Fe,Si,Zr}$. This reaction refers to the precipitation of β-Mg_2Si [17] and, thus, is directly linked to the addition of Si.

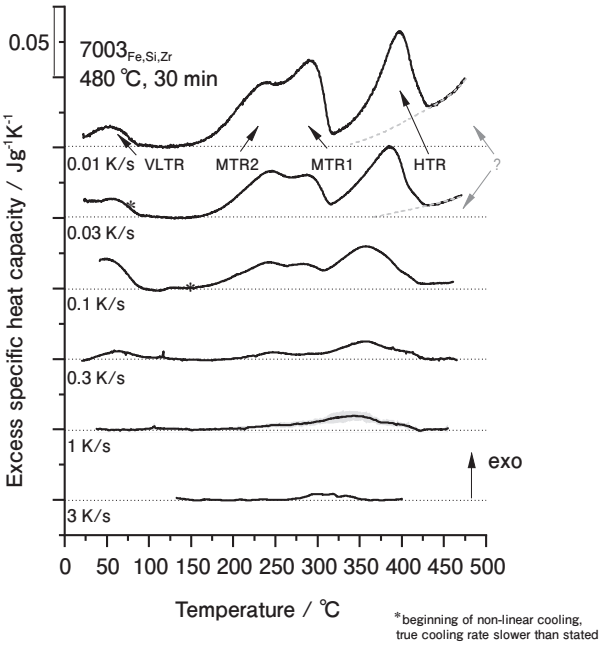

Fig. 2 Selected DSC cooling curves for $7003_{Fe,Si,Zr}$ in a range of cooling rates from 0.01 to 3 K/s.

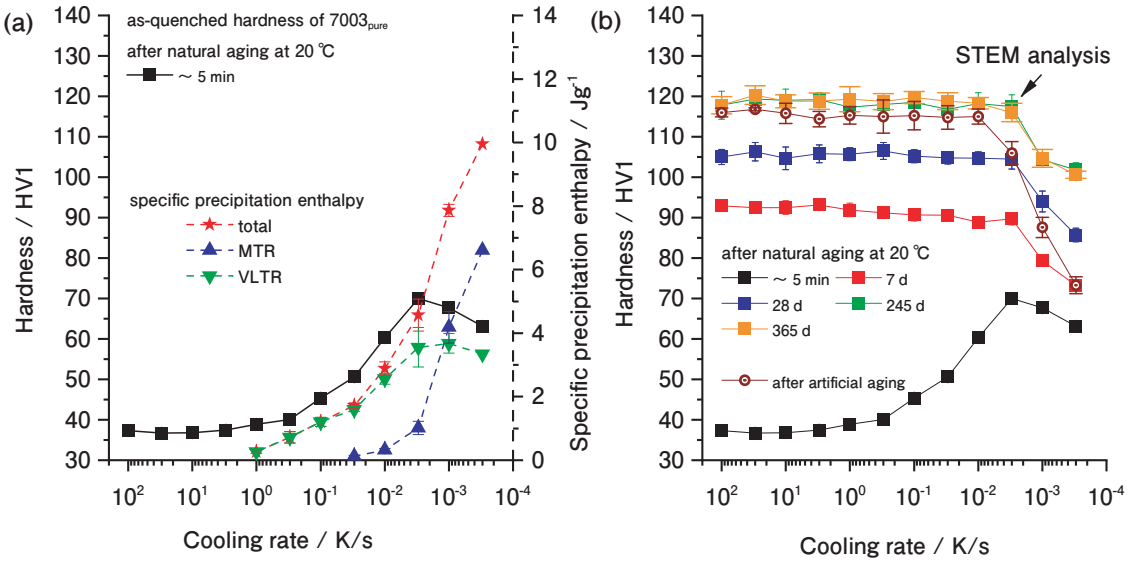

Fig. 3 7003_{pure} (a) hardness after cooling and specific precipitation enthalpy as a function of cooling rate, (b) hardness as a function of cooling rate at various natural aging durations as well as after artificial aging at 120 ℃ for 24 h.

• Secondly, it is found that in $7003_{Fe,Si,Zr}$, the MTR are present at much faster cooling rates compared to 7003_{pure}, particularly also at cooling rates at which the MTR are already fully suppressed in 7003_{pure}.

Next to these differences, there are also some aspects of QIP that are highly similar for both variants of 7003: the MTR is seen as double peak events also in $7003_{Fe,Si,Zr}$, and also the VLTR is seen in both alloys. The addition of Fe and Si adds coarse intermetallic particles enriched in Al, Si, and Fe [17], which likely form as primary particles in the melt. Those types of intermetallic particles are known to act as nucleation sites for coarse equilibrium phase QIP at high temperatures for a broad range of technical Al alloys [6]. In the case of $7003_{Fe,Si,Zr}$, particularly β-Mg_2Si nucleates on these coarse Al-Si-Fe-rich intermetallics [17]. Beyond that, the addition of Zr results in the formation of Al_3Zr dispersoids in $7003_{Fe,Si,Zr}$ [17], obviously leading to an acceleration of QIP at temperatures above 200 ℃. As a result, the VLTR is much less pronounced in $7003_{Fe,Si,Zr}$ compared to 7003_{pure}. Such VLTR has also been reported earlier for other Al-Zn-Mg alloys like 7020 and 7021 [21), 22)], and hints for such a VLTR have also been found for higher concentrated Al-Zn-Mg-Cu alloys [6), 21)]. However, as all of the latter are technical alloys and particularly contain dispersoids forming elements, such a pronounced VLTR has never been seen as in 7003_{pure}.

Also, in Fig. 2, one further aspect of the DSC methodology must be discussed: It is seen that the DSC signal at slow cooling does not start at the zero level (marked by a hash). This might be related to two different aspects: Either it could indicate a real instant precipitation reaction [19] or it might be related to a metrological DSC artifact. The latter might result from e.g., a slight variance in the surface color of the used DSC crucibles [6]. At high temperatures, part of the heat between the sensor and sample is exchanged by radiation. The surface color of the used crucibles influences the radiation emission and uptake of the sample. Here, we refrain from going deeper into this, as it does not influence the main conclusions.

3.2 Hardness and aging behavior

Fig. 3(a) plots the specific precipitation enthalpies (integrated DSC peak areas) of the MTR and the VLTR separately as well as in total for 7003_{pure}. Fig. 3(b) shows the hardness in the as-quenched condition, in naturally aged conditions after various aging durations, and after artificial aging (20 ℃ for 15 min + 120 ℃ for 24 h).

From the as-quenched hardness in Fig. 3(a), a substantial increase in hardness due to QIP is seen at rates of about 3 to 4 orders of magnitude below the full suppression of QIP. The maximum hardness in the as-quenched condition is found after cooling at 0.003 K/s to be about 70 HV1. At this cooling rate, the precipitation enthalpy of VLTR is about at its maximum, while the MTR is already suppressed to a great extent. As the precipitation enthalpy is proportional to the volume fraction precipitated by a certain reaction, it can be concluded that at a cooling rate of 0.003 K/s, a substantial fraction of precipitates is formed during the VLTR, which gives a direct hardening effect. The as-quenched hardness from 0.003 K/s toward faster cooling is decreasing due to an increasing suppression of the VLTR, which is also seen from the DSC curves and the evaluated precipitation enthalpy. The hardness in the as-quenched condition reaches a constant minimum level of about 37 HV1 for cooling at 10 K/s or faster. We conclude from that on a physical upper critical cooling rate (uCCR), which is the minimum cooling rate to achieve a complete suppression of any QIP of 10 K/s. That is a fully supersaturated solid solution is achieved after quenching with 10 K/s or faster only.

Considering the hardness after additional natural aging (Fig. 3(b)), from slowest toward faster cooling, a steep increase is seen until the cooling rate of 0.003 K/s, at which the hardness in the as-quenched condition reached its maximum. At faster rates, the hardness remains at about a constant level, which increases with prolonged duration of natural aging. After 245 days, the full aging potential of about 120 HV1 seems to be achieved. The hardness after 15 min of natural pre-aging at 20 ℃ and subsequent artificial aging at 120 ℃ for 24 h shows a similar behavior. Interestingly, the hardness level is slightly lower than after prolonged natural aging and, in particular, is only reached for cooling at 0.01 K/s or faster.

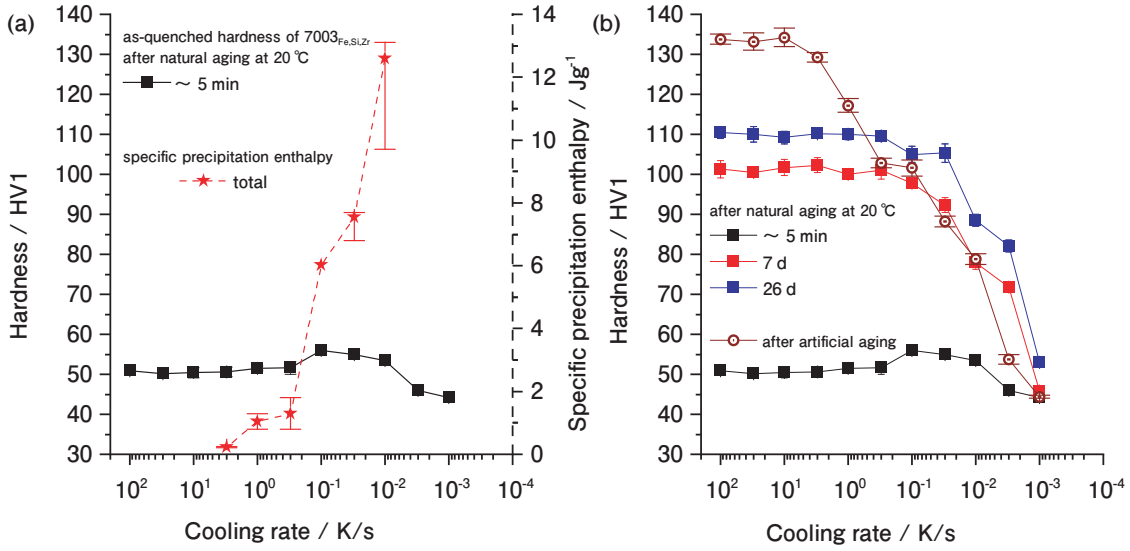

Fig. 4 $7003_{Fe,Si,Zr}$ (a) hardness after cooling and specific precipitation enthalpy as a function of cooling rate, (b) hardness as a function of cooling rate at various natural aging durations as well as after artificial aging at 120 ℃ for 24 h.

Fig. 4 shows the precipitation enthalpy as well as the hardness after natural and artificial aging as a function of cooling rate for $7003_{Fe,Si,Zr}$. Also, for this alloy, a slight peak in the as-quenched hardness is found. It is located at cooling rates about 0.01 to 0.1 K/s, at which DSC indicates the maximum of the VLTR. However, the direct hardening effect of the QIP here is way smaller compared to 7003_{pure}. The hardness after natural aging shows a saturation level for cooling at 0.1 K/s and faster. The saturation plateau for hardness after artificial aging is only reached by cooling at 10 K/s or faster. That is, for $7003_{Fe,Si,Zr}$, QIP causes negative effects in any case considering the hardness after artificial aging. In contrast, for 7003_{pure}, QIP has virtually no detrimental effect on the hardness for a wide range of cooling rates. The substantial difference can largely be attributed to the acceleration of QIP by the addition of Fe, Si, and Zr and, thereby, the addition of coarser heterogeneous nucleation sites.

A basically similar direct aging effect of quench-induced precipitates has previously been found in Al-Zn-Mg-Cu alloys [23)~25)]. The high aspect ratio Y phase platelets, enriched in Cu and Zn, was found to contribute about 50 to 100 MPa to the ultimate tensile strength in certain conditions slower cooled than the alloy specific uCCR of 300 K/s. In 23), it was revealed that the Y phase is related to precipitation during cooling in a temperature range of about 270 to 150 ℃, which is much higher compared to the VLTR seen in the case of 7003_{pure}. It is thus likely that the direct hardening effect of quench- induced precipitation seen in 7003 is caused by another type of phase.

One important general aspect of precipitation during age hardening should be addressed: according to text-book knowledge (e.g. [3), 26)]), quenched-in and, thereby, supersaturated vacancies play an important role for the diffusive mass-transport during the process of precipitation. From this work, it can be seen that precipitation during natural aging after very slow cooling has a very similar kinetic behavior compared to a preceding fast quenching. This raises the question of whether a certain critical cooling rate specifically valid for the supersaturation of the matrix by quenched-in vacancies exists. However, the aspect of the kinetics of vacancy supersaturation by quenching is not sufficiently understood and should be analyzed in future work.

3.3 Micro- and nanostructure

Fig. 5 gives an overview on the QIP visible in OM for 7003_{pure} at various cooling rates ranging from 0.0003 to 0.1 K/s. It can be seen that the coarse precipitates formed during cooling decrease in size with increasing cooling rate. At slow cooling rates, the precipitates grow to sizes of a few microns and even up to few tens of microns at grain boundaries.

Fig. 6 highlights some distinct features of coarser

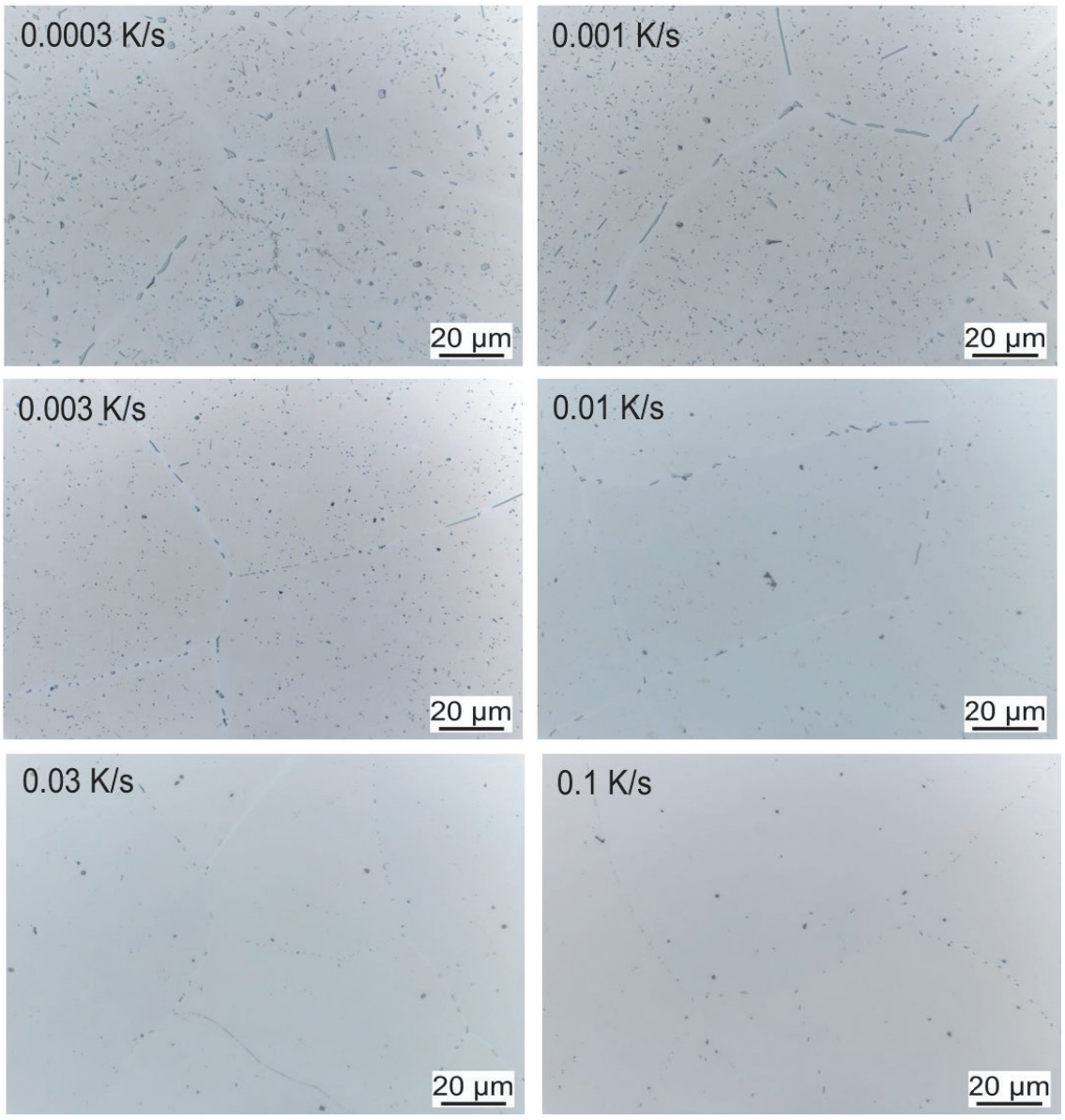

Fig. 5 Images from optical microscopy after continuous cooling of 7003_{pure} at various rates; etched with Weck's reagent (4 s).

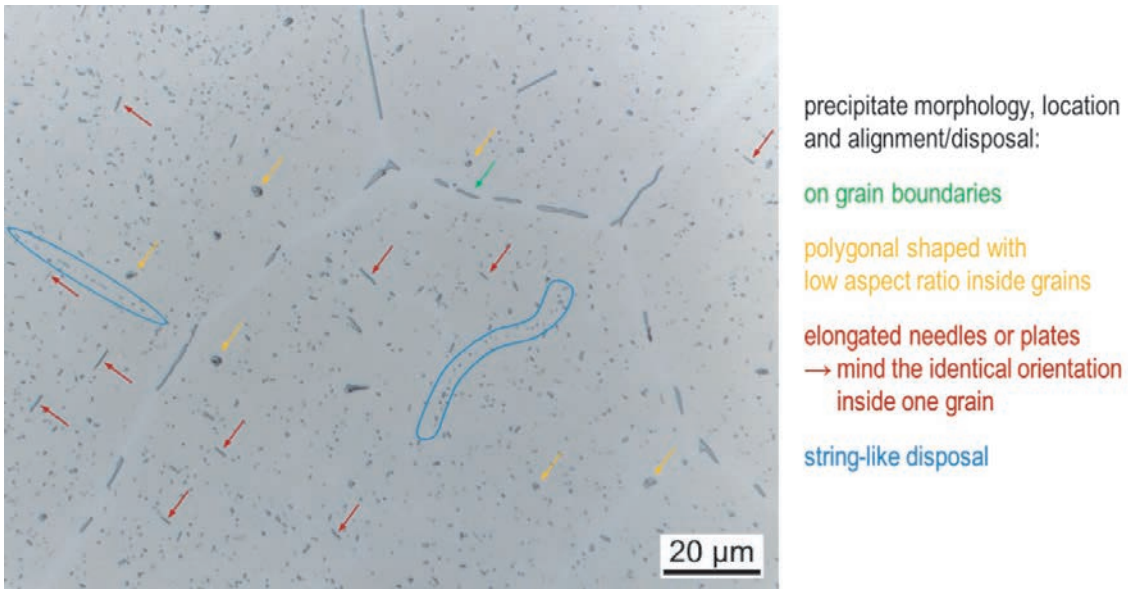

Fig. 6 Highlighting some specific features of coarse quench-induced precipitates in 7003_{pure} cooled at 0.001 K/s.

quench-induced precipitate particles, their location, and morphology. As common for most Al alloys [6], coarser quench-induced precipitates are present at grain boundaries and inside the grains much more frequently. Inside the grains, QIP occurs in two distinct morphologies: polygonal precipitates with a low aspect ratio as well as elongated rods (which potentially are plates), which have much larger aspect ratios. The rod-shaped particles appear to grow in distinct directions of the Al matrix lattice, as they often are seen parallel or perpendicular to each other within one specific grain.

With the increased magnification of scanning electron microscopy, some smaller precipitates (sub-micrometer scale) next to the coarse precipitates (μm scale) can be seen in the grain interior, which particularly holds for the slowest investigated cooling condition of 0.0003 K/s (see **Fig. 7**). They are hardly seen at faster cooling rates in SEM. On samples cooled at 0.03 and 0.1 K/s, it appears that this finer level of QIP is localized. Particularly around the coarse QIP, a depletion of such finer particles is seen, giving an impression of the area or depleted concentration of the alloying element atoms resulting from the diffusion field from which the coarse particles have grown. The radius of the diffusion field

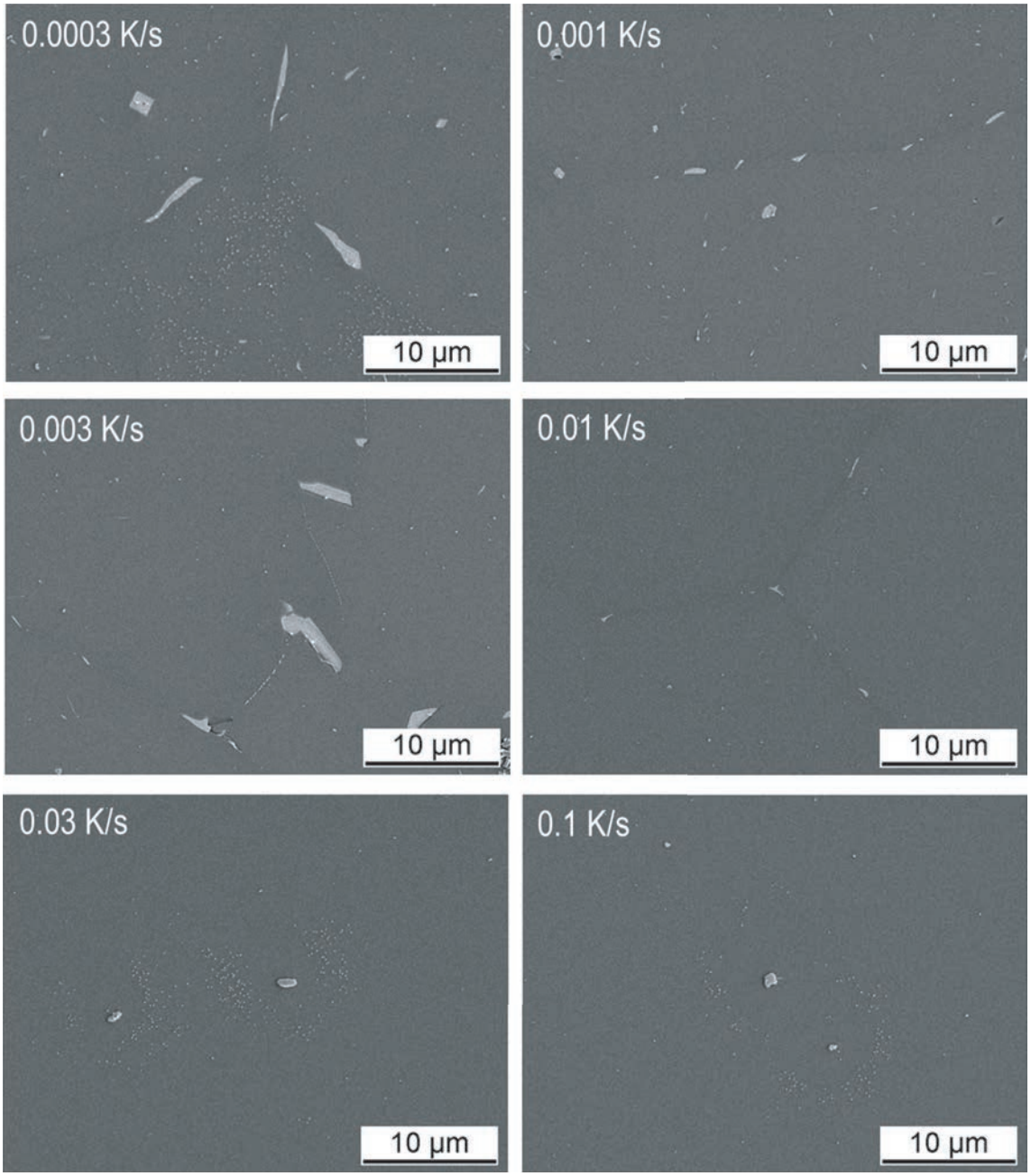

Fig. 7 SEM secondary electron images after continuous cooling of 7003_{pure} at various rates.

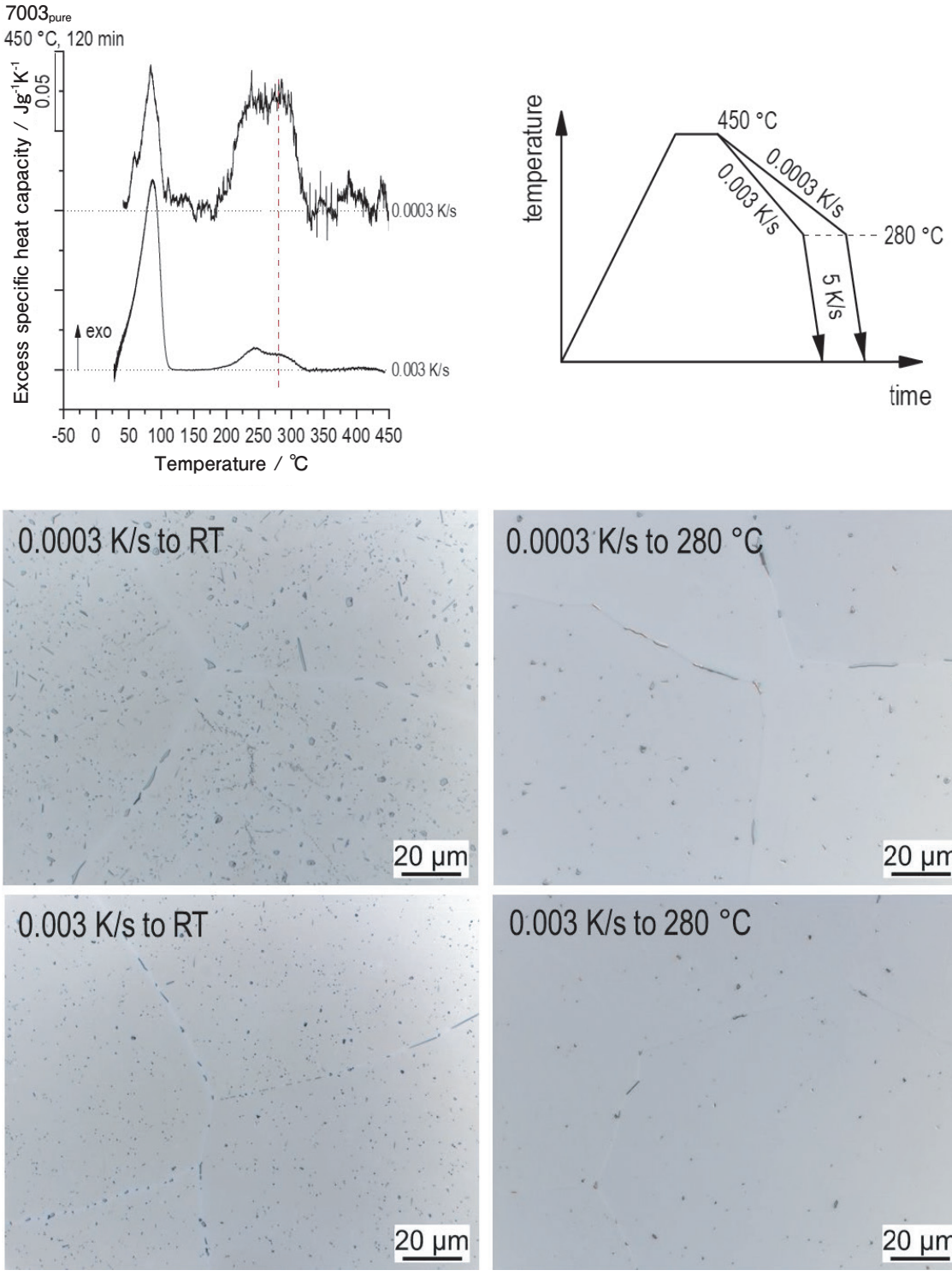

Fig. 8 Interrupted quenching method and images from optical microscopy of 7003_{pure} after interrupted quenching method; etched with Weck's reagent (4 s).

is on the order of a few microns at 0.03 and 0.1 K/s.

To gain more evidence of which types of particles grow during the precipitation events in DSC, some slow cooling experiments were interrupted shortly after the first peak of the MTR is passed (see the schematic illustration in **Fig. 8**). Samples were cooled slowly until 280 ℃ followed by an overcritical quenching at 5 K/s (overcritical in terms of the MTR). From the OM images, it can be seen that the higher temperature part of the double MTR peak refers to grain boundary precipitation and precipitation of low aspect ratio particles inside the grain. The elongated particles with a larger aspect ratio are precipitating primarily during the lower temperature part of the

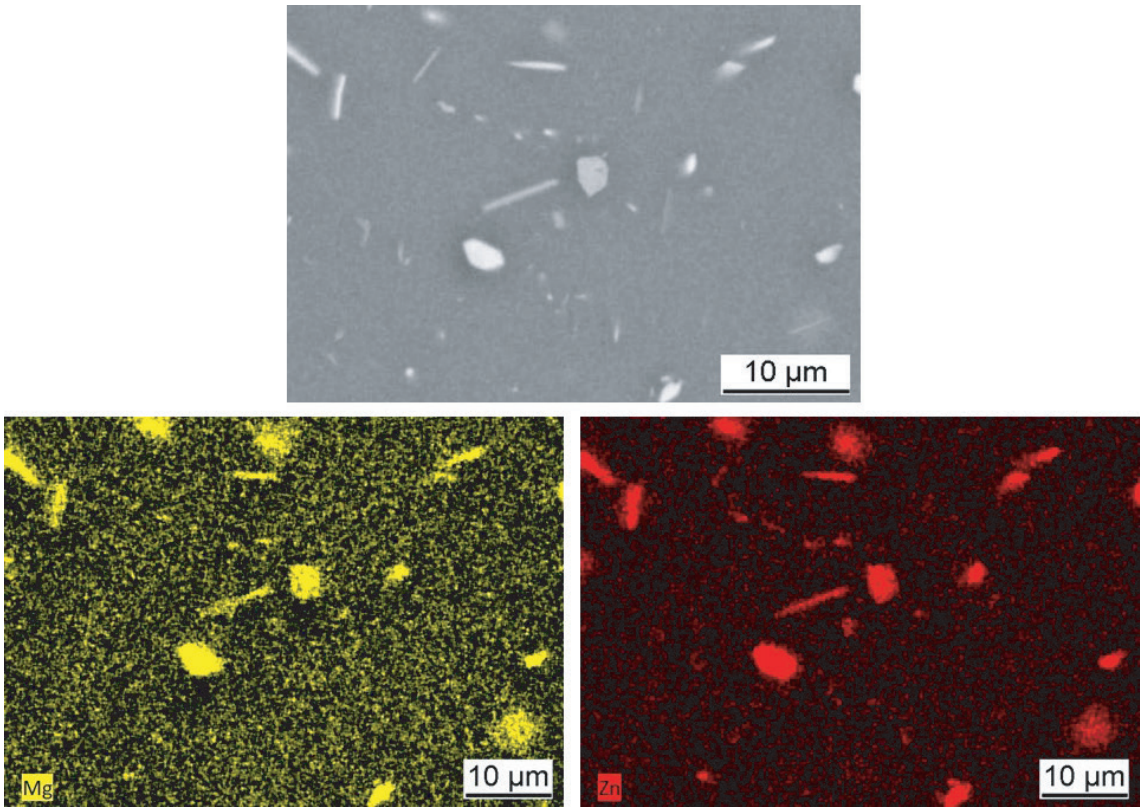

Fig. 9 SEM SE image and corresponding EDS-maps of the Zn and Mg distribution in coarse quenched induced precipitates in 7003_{pure} after slow cooling at 0.0003 K/s.

MTR. However, it is obvious that both parts are greatly overlapping. A very similar precipitation behavior has been reported earlier for the QIP of diamond cubic Si in a pure binary Al-0.72%Si alloy. In that case, Si at higher temperatures precipitated as polygonal particles with a low aspect ratio, while the same phase precipitated as thin plates with a largely increased aspect ratio at lower temperatures [6), 27)].

The SEM–EDS in **Fig. 9** clearly indicates an enrichment in Mg and Zn for all types of coarse QIP from slow cooling at 0.0003 K/s. Additional XRD analysis (spectra not shown) of a sample cooled at the same rate gives evidence for the presence of the -$MgZn_2$ phase, which might contain different Al content, as has been discussed in several studies [28), 29)].

STEM analysis was done on a 7003_{pure} sample cooled at 0.003 K/s to room temperature. The cooled sample was aged at room temperature for about 9 months before a TEM foil was prepared from it. From the HAADF-STEM images in **Fig. 10**, an enormous number density of nanoparticles is seen. The nanoparticles appear globular, and their diameters are found to be about 2 to 4 nm. STEM-EDS revealed an enrichment in Zn and Mg also for the clusters, while Al is depleted. As the sample was naturally aged for some months prior to the TEM foil preparation, the structures seen are a result of cooling and aging. However, as the hardness directly after cooling shows a peak, one can assume that they have partly grown during cooling.

As a summarizing result, a continuous cooling precipitation diagram for 7003_{pure} can be constructed from the DSC, hardness, and microstructures **(Fig. 11)**. The separation of the double peak during the medium temperature reaction is plotted with a dashed line, as it is hard to determine due to the overlap of the two reactions involved. Additionally, the uCCR of the very low temperature reaction is estimated by the hardness results for a cooling rate of 10 K/s. That is, when the hardness after artificial aging does not increase with increasing cooling rate, the very low temperature reaction should be suppressed completely.

The continuous cooling precipitation diagram for $7003_{Fe,Si,Zr}$ is shown in **Fig. 12**. It contains Mg_2Si precipitation as a further HTR. Only clearly determinable reactions were drawn with a solid line. Uncertain reaction temperatures due to the severe

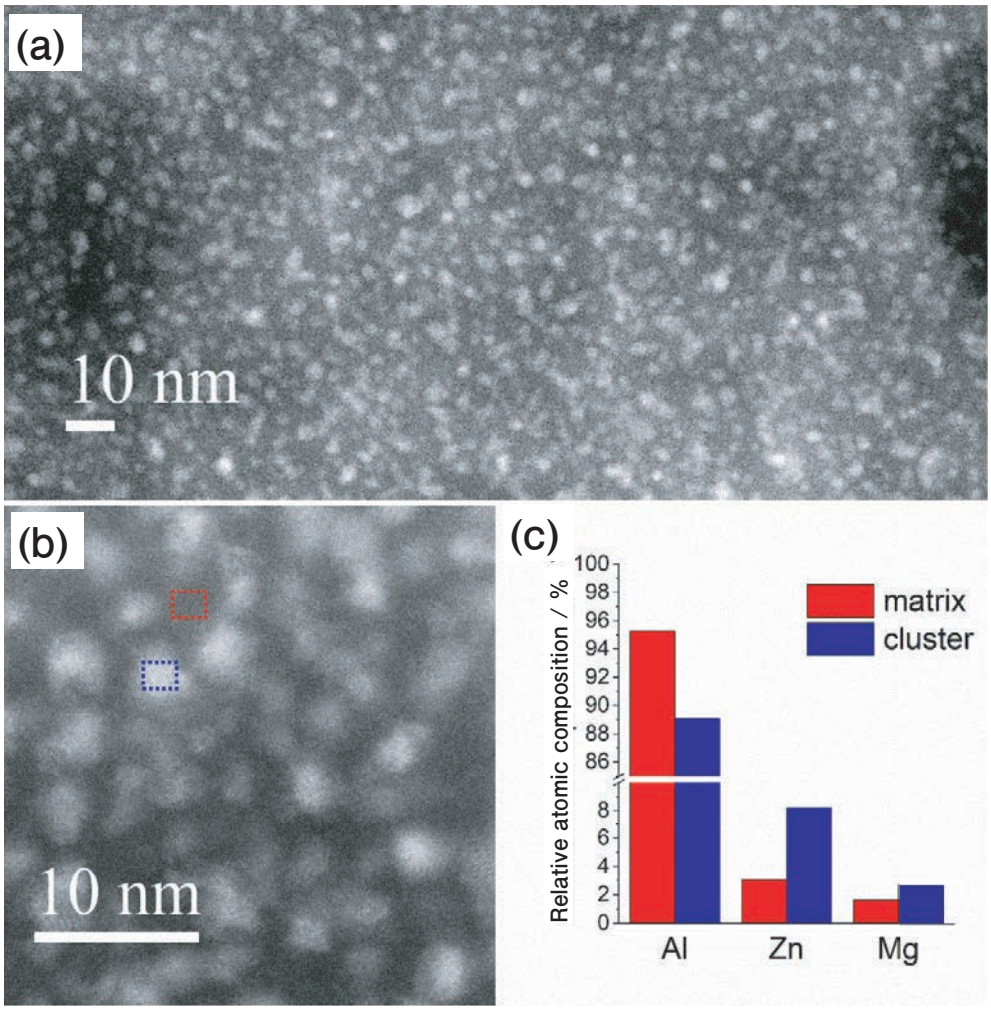

Fig. 10 (a), (b) HAADF-STEM images indicating an enormous number density of nanoparticles after cooling at 0.003 K/s and natural aging for about 9 months. (c) Relative atomic composition from EDS comparing only the elements Al, Mg, and Zn of the two areas highlighted in b indicating a clear enrichment of the clusters in Mg and particularly in Zn.

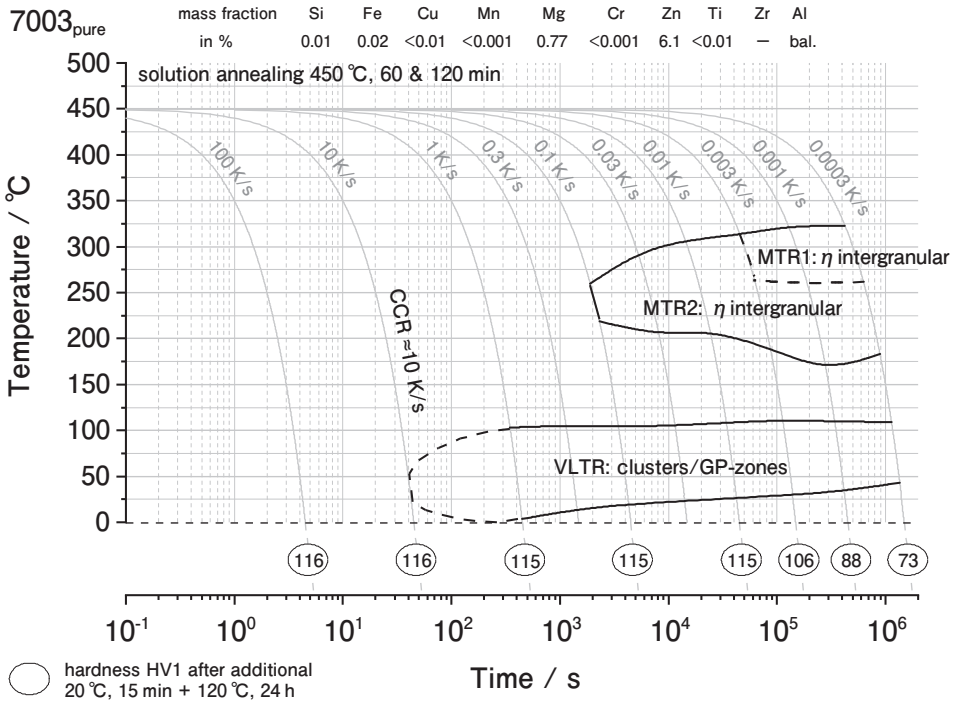

Fig. 11 Continuous cooling precipitation diagram of 7003_{pure}.

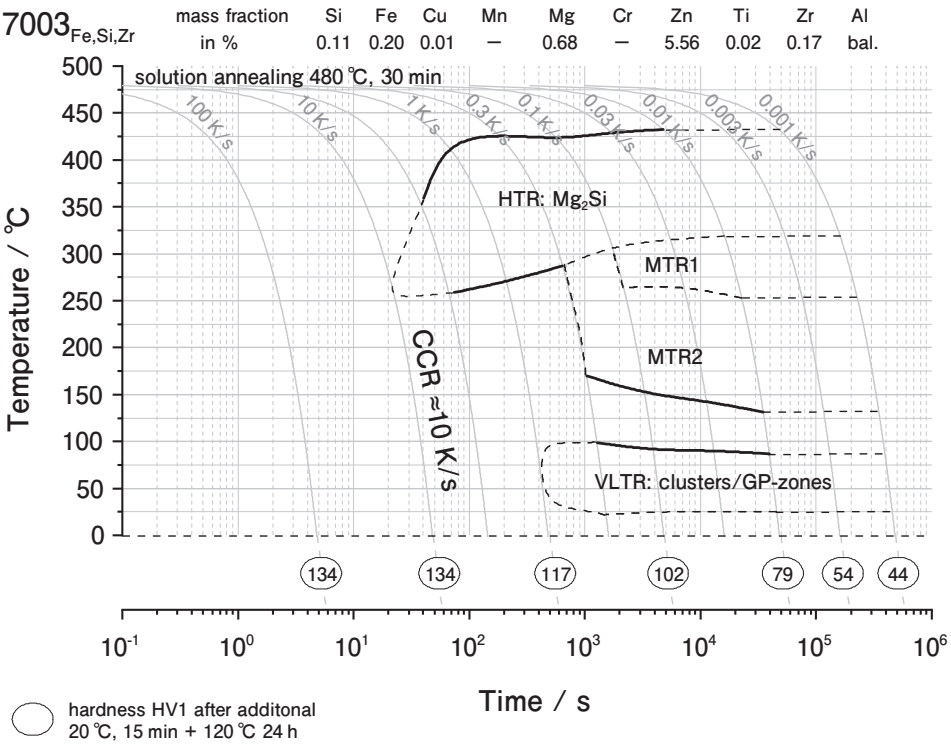

Fig. 12 Continuous cooling precipitation diagram of $7003_{Fe,Si,Zr}$.

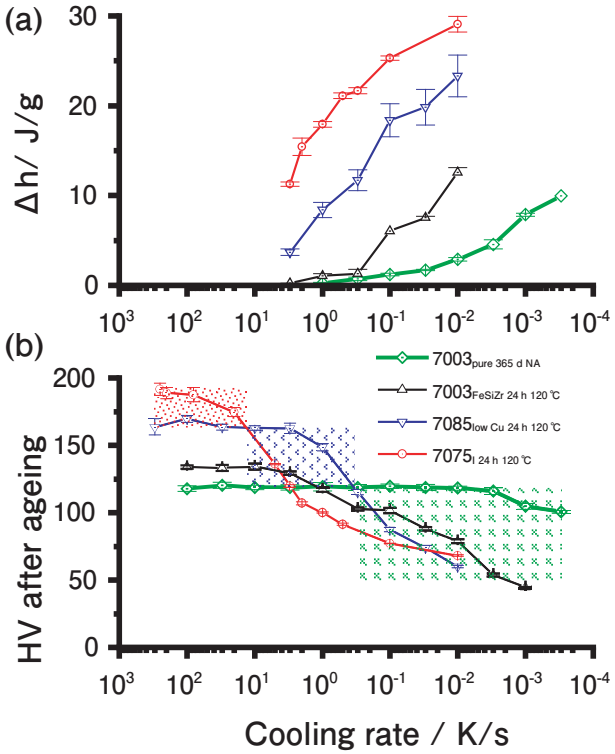

Fig. 13 (a) Specific total precipitation enthalpy during cooling from solution treatment and (b) hardness after cooling and subsequent aging for four different Al-Zn-Mg-(Cu) alloys over a broad range of cooling rates. The data of 7075_I and 7085 have been taken from literature [6), 30)].

overlap were plotted as a dashed line.

Fig. 13 compares the total specific precipitation enthalpies released during cooling and the hardness after subsequent aging for four Al-Zn-Mg(-Cu) alloys. These four alloys are largely different in the concentration of the main alloying elements as well as elements forming primary precipitates and dispersoids (for details on the alloys $7085_{low\ Cu}$ and 7075_I see Refs. 6) and 30)). Therefore, the amount of nucleation sites for coarse heterogeneous nucleation of quench-induced precipitation differs. It is seen that the alloy 7075_I might lead to maximum possible hardness values, but this is only true if very fast cooling at about 300 K/s can be applied. $7085_{low\ Cu}$ and especially 7003_{pure} come along with slower precipitation kinetics during quenching, which results in higher strength at lower cooling rate ranges. This might be important if the cooling rate is restricted due to technological reasons (thick components or for distortion control).

4. Conclusions

Based on in situ cooling DSC covering four orders of magnitude in cooling rate (0.0003 to 1 K/s) and correlative hardness testing as well as structure analysis by optical and electron microscopy on an Al-6%Zn-0.75%Mg alloy without (7003_{pure}) and with minor additions of Fe, Si, and Zr ($7003_{Fe,Si,Zr}$), we

conclude the following:

• Quench-induced precipitation (QIP) in 7003_{pure} happens in two distinct main reaction temperature regions: a medium temperature reaction (MTR, about 330 ℃ to 175 ℃) and a very low temperature reaction (VLTR, about 110 ℃ to 10 ℃); for cooling rates faster than 0.003 K/s, the majority of the transformed enthalpy is released by the VLTR. Such a VLTR has been seen for other alloys before, but is much more pronounced in this alloy.

• Small additions of Fe, Si, and Zr (in sum less than 0.3at.%) have a severe influence on the QIP: the addition of Si adds the sequence of Mg_2Si seen as an additional high temperature reaction in the DSC for $7003_{Fe,Si,Zr}$. and by adding additional nucleation sites (as coarsepotentially primary – Fe-, Si-rich intermetallics or as Al_3Zr- dispersoids). In particular, the Al_3Zr dispersoids, which were already previously known as nucleation sites for the QIP of the η-$Mg(Zn,Al)_2$-phase, accelerate its precipitation and, thus, substantially increase the quench sensitivity.

• The MTR originates from the superposition of two largely overlapping reactions. It is most likely that these different contributions originate from the precipitation of the same η-$Mg(Zn,Al)_2$-phase precipitating from different nucleation sites and in different morphologies. At slightly higher temperatures, the η-$Mg(Zn,Al)_2$-phase precipitates on grain boundaries and inside the grains as polygonal shaped particles with a low aspect ratio. At slightly lower temperatures, precipitation of the η-$Mg(Zn,Al)_2$-phase occurs in rod-shaped particles with a largely increased aspect ratio. In all cases, the η-$Mg(Zn,Al)_2$-phase particles reach dimensions ranging from several tens of microns down to some hundreds of nm depending on the cooling rate.

• The VLTR refers to the formation of a huge particle number density of nanoparticles. Those apparently are globular with a diameter of about 3 to 5 nm after cooling at 0.003 K/s and additional natural aging for some months. Those quenched-in nanoparticles gain a substantial direct hardening contribution, and the hardness in the as-quenched condition shows a maximum at 0.003 K/s.

• For 7003_{pure} in a broad range of cooling rates (0.003 to 10 K/s), the QIP is found to cause no negative effect on the hardness after natural aging. For this alloy, the hardness after natural aging for 9 month or longer is found to be on the saturation level of about 120 HV1 for cooling rates above 0.003 K/s (i.e., cooling durations shorter than about 40 h). Therefore, for this alloy, we distinguish a technical critical cooling rate (tCCR, in terms of hardness) to be 0.003 K/s, while a full supersaturation of the solid solution is reached with the physical upper critical cooling rate of 10 K/s.

Acknowledgements

The Jeol NeoARM STEM was funded by the German Research Foundation (Deutsche Forschungsgemeinschaft) DFG INST 264/161-1 FUGG.

Dr. Carsten Kreyenschulte and Dr. Markus Frank are gratefully acknowledged for their help with the electron microscopy analysis and related discussions.

Author contribution

BM and CR conceived the experimental plan. MMN produced the material under the guidance of HY and KY; CR did the DSC analysis; AS did the SEM analysis; KO and BM did the STEM analysis; all authors contributed to the discussion of the data. BM and CR wrote the raw manuscript; OK did the final revision. All authors approved the final version of the manuscript.

REFERENCES

1) T. Dursun and C. Soutis: Mater. Des. (1980-2015), **56** (2014), 862-871.
2) J. Shin, T. Kim, D. Kim, D. Kim, K. Kim: J. Alloys Compd. **698** (2017), 577-590.
3) I. J. Polmear: Light alloys: from traditional alloys to nanocrystals, 4th edn. Elsevier Butterworth-Heinemann, Amsterdam (2006).
4) P. A. Rometsch, Y. Zhang, S. Knight: Trans Nonferrous Met. Soc. China, **24** (2014), 2003-2017.
5) K. Strobel, M. A. Easton, L. Sweet, M. J. Couper, and N. F. Nie: Mater. Trans., **52** (2011), 914-919
6) B. Milkereit, M. J. Starink, P. A. Rometsch, C. Schick, O. Kessler: Materials, **12** (2019)
7) H. Yoshida: Proceedings 12th international conference on aluminum alloys, The Japan Institute of Light Metals, Yokohama, Japan, (2010), 54-61.
8) Y. Baba: J. Jpn. Inst. Met., **31** (1967), 910-915.

9) Y. Baba: Trans. JIM, **11** (1970), 404-410.
10) Y. Baba and H. Yoshida: Recent development of 7003 extrusion alloy. Proceed Second Int Aluminum Extrusion Technol Semin 1 (1977), 301-306
11) Y. Baba, T. Fukui, A. Takashima and S. Terai: 6th international conference on light metals-Leoben/Vienna, (1975), 99-101
12) Y. Baba, T. Fukui, A. Takashima: J. Japan Inst. Light Metals, **24** (1974), 25-35.
13) Y. Baba: Sumitomo Light Metal Tech. Rep., **41** (2000), 91-121.
14) H. Yoshida and Y. Baba: J. Japan Inst. Light Metals, **31** (1981), 20-29.
15) Y. Zhang, C. Bettles and P. A. Rometsch: J. Mater. Sci., **49** (2014), 1709-1715.
16) T. A. Pan, Y. C. Tzeng, H. Y. Bor, K. H. Liu and S. L. Lee: Materials Today Communications, **28** (2021), 102611.
17) A. Lervik, C. D. Marioara, M. Kadanik, J. C. Walmsley, B. Milkereit and R. Holmestad: Mater. Des., **186** (2020), 108204.
18) H. Yoshida, T. Watanabe and H. Hatta: Mary Wells MB (ed) 16th International Conference on Aluminium Alloys, Montreal, Canada. METSOC.org, (2018), paper 393778.
19) R. H. Kemsies, B. Milkereit, S. Wenner, R. Holmestad and O. Kessler: Mater. Des. **146** (2018), 96-107.
20) E. Weck and E. Leistner : Metallographische Anleitung zum Farbätzen nach dem Tauchverfahren Teil III: Nichteisenmetalle, Hartmetalle und Eisenwerkstoffe. Deutscher Verlag für Schweisstechnik, Düsseldorf, Nickel-Basisund Kobalt-Basis-Legierungen (1986).
21) Y. Zhang, B. Milkereit, O. Kessler, C. Schick and P. A. Rometsch: J. Alloys Compd., **584** (2014), 581-589.
22) B. Milkereit, M. Osterreich, P. Schuster, G. Kirov, E. Mukeli and O. Kessler: Metals, **8** (2018), 531.
23) Y. Zhang, M. Weyland, B. Milkereit, M. Reich, P. A. Rometsch: Sci. Rep., **6** (2016), 23109.
24) S. Liu, Q. Li, H. Lin, L. Sun, T. Long, L. Ye and Y. Deng Y: Mater. Des., **132** (2017), 119-128.
25) S. Liu, M. Zhang, Q. Li, Q. Zhu, H. Song, X. Wu, L. Cao and M. J. Couper: Mater. Sci. Eng. A, **793** (2020), 139900.
26) F. Ostermann: Anwendungstechnologie Aluminium, 3rd edn., Springer-Verlag, Berlin, (2014).
27) P. Schumacher: Plastisches verformungsverhalten unterkü hlter aluminiumlegierungen im system Al-Mg-Si. PhD thesis, Universität Rostock, (2018).
28) X. Fang, M. Song, K. Li, Y. Du, D. Zhao, C. Jiang and H. Zhang: J. Mater. Sci., **47** (2012), 5419-5427.
29) P. Liang, T. Tarfa, J. A. Robinson, S. Wagner, P. Ochin, M. G. Harmelin, H. J. Seifert, H. L. Lukas and F. Aldinger: Thermochim Acta, **314** (1998), 87-110
30) M. J. Starink, B. Milkereit, Y. Zhang and P. A. Rometsch: Mater. Des., **88** (2015), 958-971.

Christian Rowolt
Chair of Materials Science, Faculty of Mechanical Engineering and Marine Technology, University of Rostock, Ph. D.
Competence Centre CALOR, Department Life, Light & Matter, University of Rostock

Benjamin Milkereit
Chair of Materials Science, Faculty of Mechanical Engineering and Marine Technology, University of Rostock, Ph. D.
Competence Centre CALOR, Department Life, Light & Matter, University of Rostock
Centre for Interdisciplinary Electron-Microscopy (ELMI-MV), Department Life, Light and Matter, University of Rostock

Mami Mihara-Narita
Department of Physical Science and Engineering, Nagoya Institute of Technology, Ph. D.

Hideo Yoshida
ESD Laboratory, Dr. Eng.
Formerly, Adviser,
Research & Development Division,
UACJ Corporation

Kenya Yamashita
Furukawa UACJ Memory Disk Co., Ltd., Ph. D.

Olaf Kessler
Chair of Materials Science, Faculty of Mechanical Engineering and Marine Technology, University of Rostock, Ph. D.
Competence Centre CALOR, Department Life, Light & Matter, University of Rostock
Centre for Interdisciplinary Electron-Microscopy (ELMI-MV), Department Life, Light and Matter, University of Rostock